Numerical simulations of a falling film on the inner surface of a rotating cylinder

U. Farooq [1,*] J. Stafford [1,2] C. Petit,[1] and O. K. Matar [1,†]

[1]*Department of Chemical Engineering, Imperial College London, London SW7 2AZ, United Kingdom*
[2]*School of Engineering, University of Birmingham, B15 2TT, United Kingdom*

A flow in which a thin film falls due to gravity on the inner surface of a vertical, rotating cylinder is investigated. This is performed using two-dimensional (2D) and 3D direct numerical simulations, with a volume-of-fluid approach to treat the interface. The problem is parameterized by the Reynolds, Froude, Weber, and Ekman numbers. The variation of the Ekman number (Ek), defined to be proportional to the rotational speed of the cylinder, has a strong effect on the flow characteristics. Simulations are conducted over a wide range of Ek values ($0 \leqslant \text{Ek} \leqslant 484$) in order to provide detailed insight into how this parameter influences the flow. Our results indicate that increasing Ek, which leads to a rise in the magnitude of centrifugal forces, produces a stabilizing effect, suppressing wave formation. Key flow features, such as the transition from a 2D to a more complex 3D wave regime, are influenced significantly by this stabilization and are investigated in detail. Furthermore, the imposed rotation results in distinct flow characteristics such as the development of angled waves, which arise due to the combination of gravitationally and centrifugally driven motion in the axial and azimuthal directions, respectively. We also use a weighted residuals integral boundary layer method to determine a boundary in the space of Reynolds and Ekman numbers that represents a threshold beyond which waves have recirculation regions.

I. INTRODUCTION

Falling liquid films are of central importance to a range of industrial applications and associated unit operations, which include reactors, distillation columns, heat exchangers, condensers, and evaporators. It is unsurprising, therefore, that they have enjoyed significant attention in the literature for several decades since the seminal work of Kapitza [1–4]. Falling film flows are characterized by complex dynamics and pattern formation. Waves emerge naturally from disturbances near the inlet, which then grow downstream and as their amplitude increases, nonlinearities then give rise to growth saturation; the resulting wave deceleration then leads to constant wave speed. Two distinct types of waves have been detected corresponding to short waves that are nearly sinusoidal in shape, typically found near the flow inlet, and longer, large-amplitude, solitary waves, further downstream; the latter have tall, well-separated peaks, which are preceded by capillary waves of much smaller amplitude and whose speed is maintained by the constant compression from the main solitary wave peak, located immediately upstream [5]. The interfacial dynamics are also accompanied by transitions from two- (2D) to three-dimensional waves that resemble horseshoe-like coherent structures, and at higher film Reynolds numbers, "roll waves" overtake the capillary waves resulting in complex, apparently random, wave structures [4,6].

Numerous methods have been employed to investigate the behavior of thin falling films. Experimentally, film thicknesses and velocity profiles can be determined through laser-based techniques including fluorescence and particle image velocimetry measurements [7–13]. Furthermore, modeling and numerical simulations have been used extensively to provide insight into the complex falling film dynamics. Low-dimensional (LD) modeling, whereby the governing equations and boundary conditions are simplified, such as the weighted residual integral boundary layer (WRIBL) model by Ruyer-Quil and Manneville [14] have been used to provide an accurate representation of the hydrodynamics. A comparison of these models is perfomed by Scheid *et al.* [15]. Numerical modeling and direct numerical simulations (DNS) have also been deployed starting with the work of Ramaswamy *et al.* [16] who were among the first to perform DNS on falling liquid films, using a finite-element method with a Lagrangian-Eulerian formulation to analyze the spatial and temporal stability of the flow. Two-dimensional simulations of falling films using the volume-of-fluid method were performed by Gao *et al.* [17], who examined the time-space wave evolution at different Reynolds and Weber numbers. Gao *et al.* [17] and Nosoko and Miyara [18] also assessed the impact of forcing the inlet flow rate with certain frequencies on the emergent wave formation, an approach similar to that employed experimentally by Park *et al.* [19]. Recently, Denner *et al.* [20] compared experimental measurements with DNS and LD modeling for solitary waves on inertia-dominated falling liquid films, finding good agreement. These authors have further investigated the onset of recirculation within the waves whose presence acts to intensify the rates of heat and mass transfer in the falling film [21–24].

*usmaan.farooq13@imperial.ac.uk
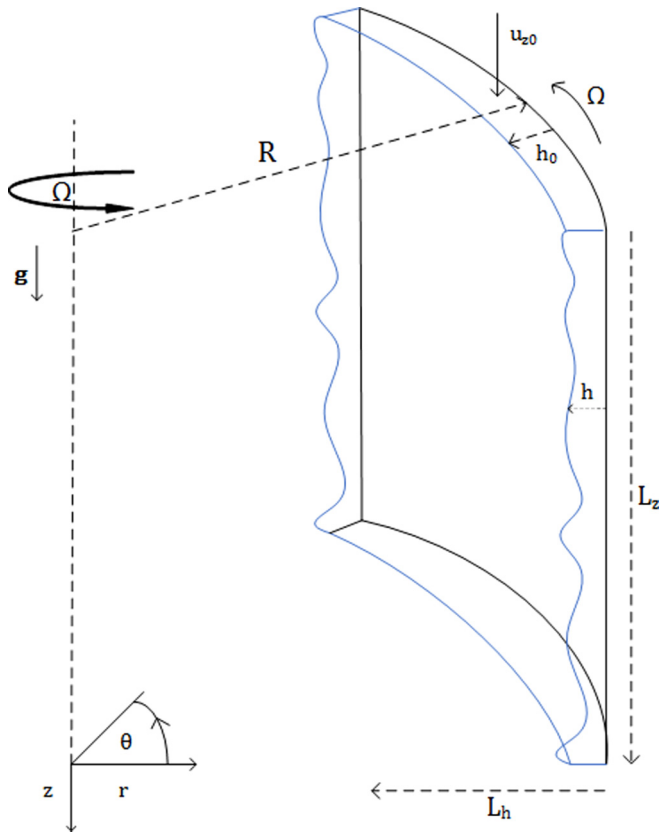†o.matar@imperial.ac.uk

FIG. 1. Schematic of the flow showing fluid entering through an inlet at the top of a cylinder of radius R, with velocity u_{z0} and height h_0, adhering to the cylinder wall which rotates at constant speed Ω, resulting in a film with height, $h = R - r$. The computational domain has lengths L_z and L_h in the axial and radial directions, and covers a $90°$ cylinder sector in the azimuthal direction.

In the present work, we consider the dynamics of a film falling under gravity on the inside of a cylinder, which is undergoing steady rotation; this study is carried out in connection with applications such as evaporators in which the rotation provides an additional degree of freedom to intensify heat and mass transfer rates [25]. Notably, it has been shown that the rotation increases the heat transfer coefficients by 25% in the case of a centrifugal thin-film evaporator, while even greater increases are found in other geometries such as spinning disks [26,27]. Furthermore, rotation provides greater control over the flow dynamics in comparison to the nonrotating falling film case. It is also noteworthy that the problem of a rotating, thin falling film is related to that involving a thin-film flow down an inclined plane; in both flows, the films are influenced by a body force, which corresponds to centrifugation and gravity in the rotating and nonrotating cases, respectively. In the inclined plane case, for angle γ above the horizontal, the Kapitza instability, which eventually leads to wave formation, as described above, is present for $\mathrm{Re} > 5/6 \cot \gamma$ [28,29]. For angles past the vertical, the films, which are on the underside of an inclined plane, are also vulnerable to a Rayleigh-Taylor instability [30], as summarized in Fig. 1 of Rietz et al. [31].

If one considers the forces acting on the system, then the gravity component can be separated into a contribution

in the streamwise direction and one normal to this into the plane. Inertia and the streamwise gravity component serve to destabilize the flow, whereas surface tension and the gravity component normal to the flow have a stabilizing effect. This is comparable to the current case, in which the normal component of gravity in the inclined plane case plays the role of the centrifugal force due to rotation of the cylinder. Thus, the angle of inclination can be equated to the ratio of the centrifugal and gravitational accelerations. Rietz et al. [31] have made use of this parameter to classify the results of their experimental study of thin-film flow on the outside of a vertical, rotating cylinder that feature the formation of 2D and 3D waves, rivulet formation, and dripping.

Linear stability analyses of a thin film on the surface of a rotating cylinder have been performed by Chen et al. [32] and Davalos-Orozco et al. [33] using the lubrication approximation. Davalos-Orozco et al. [33] have noted that for flow on the inside of the cylinder, inertial, and capillary forces have a destabilizing effect, whereas the centrifugal force stabilizes the flow. From this analysis, a critical, so-called centrifugal number can be determined, suggesting that the flow is stable for a sufficiently large rotational speed.

Although films falling on the exterior of a rotating cylinder have rich dynamics due to the simultaneous presence of Kapitza, Rayleigh-Taylor, and centrifugal instabilities [31,34,35], we focus on the effect of the stabilizing centrifugal force associated with flow on the inner surface of a rotating cylinder. In contrast to Rietz et al. [31] where the flow was on the outside of the cylinder, and the centrifugal force served to destabilize the flow by forcing fluid away from the cylinder wall, here the flow is on the inner surface of the cylinder. Therefore, the centrifugal force acts on the fluid by forcing it toward the cylinder wall and suppressing wave formation. This force will act in competition with the destabilizing gravitational force that leads to the Kapitza instability. Notably the centrifugal force is weakest at the crest of the waves making this region more susceptible to instabilties. Here we will perform a numerical investigation of the flow, which is yet to be studied in the nonlinear regime beyond the onset of linear instabilities [33,36,37]. The role that rotation has on the dynamics and stability of the flow will be examined and our results will demonstrate the emergence of large-amplitude waves that travel at a well-defined angle to the axis of the vertical cylinder.

The rest of this paper is organized as follows: In Sec. II, the problem formulation is presented, highlighting the key nondimensional parameters associated with the flow via scaling of the governing equations; a brief exposition of the numerical methods deployed is also provided. In Sec. III, the results from two-dimensional simulations, within a rotating frame of reference, are presented, while in Sec. IV, the predictions from the three-dimensional simulations are discussed. Finally, conclusions and an outlook for future work are presented in Sec. V.

II. PROBLEM FORMULATION

We consider a Newtonian liquid film of density ρ_l and viscosity μ_l flowing due to gravity down the inner surface of a rigid and impermeable cylinder of radius R, oriented vertically, and rotating with a constant angular velocity Ω.

A gas phase of density ρ_g and viscosity μ_g is also present in the cylinder, and the gas and liquid phases are separated by an interface with surface tension σ. We use cylindrical coordinates, r, θ, and z, defined as shown in Fig. 1, with associated velocity components, u_r, u_θ, and u_z, to describe the flow. The film has thickness $h(\theta, z, t)$ such that the gas-liquid interface is located at $r = R - h$. The fluid is considered to be incompressible, isothermal, and can be described by the continuity and momentum equations, respectively given by:

$$\nabla \cdot \mathbf{u} = 0, \tag{1}$$

$$\rho \left(\frac{\partial \mathbf{u}}{\partial t} + \mathbf{u} \cdot \nabla \mathbf{u} \right) = -\nabla p + \mu \nabla^2 \mathbf{u} + \rho g \hat{\mathbf{z}} + \sigma \kappa \mathbf{n} \delta, \tag{2}$$

where $\mathbf{u}$ is the velocity, p the pressure, g the gravitational acceleration, κ, the curvature of the interface, $\mathbf{n}$ the unit normal at the interface, δ represents the Dirac delta function concentrated at the interface, and $\hat{\mathbf{z}}$ is the unit vector in the z direction. Here we have used the CSF model [38] in order to model the surface tension between two fluids.

We use a volume-of-fluid (VOF) interface-capturing approach to simulate the interfacial dynamics within the open-source environment OpenFOAM. According to the VOF method, a species transport equation is used to determine the volume fraction, α, of each phase in every computational cell. The function α allows one to define the local density and viscosity as

$$\rho = \alpha \rho_g + (1 - \alpha) \rho_l, \tag{3}$$

$$\mu = \alpha \mu_g + (1 - \alpha) \mu_l, \tag{4}$$

and α is advected using the following equation:

$$\frac{\partial \alpha}{\partial t} + \nabla \cdot (\alpha \boldsymbol{u}) = 0. \tag{5}$$

The continuum surface force approach to model the surface tension force according to which the normal $\mathbf{n}$ and curvature κ are respectively expressed by

$$\mathbf{n} = \frac{\nabla \alpha}{|\nabla \alpha|}, \quad \text{and} \quad \kappa = -\nabla \cdot \left(\frac{\nabla \alpha}{|\nabla \alpha|} \right). \tag{6}$$

In order to construct a sharper interface, Eq. (5) is modified to compress the surface and reduce smearing; further details can be found in Ref. [39]. Roenby *et al.* [40], recently implemented an isoAdvector scheme within OpenFOAM, allowing for higher Courant numbers than the standard solver with MULES. This uses the concept of isosurfaces to calculate more accurate face fluxes, specifically for the cells containing the interface. This geometric method has an optimum performance at $\text{Co} \approx 0.5$, compared to $\text{Co} \leqslant 0.1$ for the algebraic VOF approach implemented in the interFoam solver [40]. This isoAdvector solver (interFlow) was used in the current study.

The governing equations are rendered dimensionless via introduction of the following scaling:

$$\tilde{\mathbf{u}} = \frac{\mathbf{u}}{u_N}, \quad \tilde{\mathbf{x}} = \frac{\mathbf{x}}{h_N}, \quad \tilde{t} = \frac{t}{h_N/u_N}, \quad \tilde{p} = \frac{p}{\rho u_N^2}, \quad \tilde{\kappa} = \frac{\kappa}{1/h_N}, \tag{7}$$

in which h_N and u_N correspond, respectively, to the Nusselt thickness and velocity for a planar falling film in the absence

of rotation:

$$h_N = \sqrt[3]{\frac{3\mu_l q_N}{\rho_l g}}, \quad u_N = \frac{\rho_l g h_N^2}{3\mu_l}, \tag{8}$$

where $q_N = h_N u_N$. Note that we have also set $\tilde{\delta} = h_N \delta$, since the δ function can be defined as $\delta = \nabla H(\mathbf{x} - \mathbf{x_s})$, where H and $\mathbf{x}_s$ are the Heaviside function and position of the interface respectively, whereby H is approximated numerically [41]. Above and below, tildes designate dimensionless variables. Applying these scalings to the mass and momentum equations, we obtain

$$\tilde{\nabla} \cdot \tilde{\mathbf{u}} = 0, \tag{9}$$

$$\frac{\partial \tilde{\mathbf{u}}}{\partial \tilde{t}} + \tilde{\mathbf{u}} \cdot \tilde{\nabla} \tilde{\mathbf{u}} = -\tilde{\nabla} \tilde{p} + \frac{1}{\text{Re}} \tilde{\nabla}^2 \tilde{\mathbf{u}} + \frac{1}{\text{Fr}^2} \hat{\mathbf{z}} + \frac{1}{\text{We}} \tilde{\kappa} \tilde{\boldsymbol{\delta}}, \tag{10}$$

where the dimensionless parameters that appear in Eq. (10) correspond to the Reynolds, Froude, and Weber numbers, respectively given by:

$$\text{Re} = \frac{\rho u_N h_N}{\mu}, \quad \text{Fr} = \frac{u_N}{\sqrt{g h_N}}, \quad \text{We} = \frac{\rho u_N^2 h_N}{\sigma}. \tag{11}$$

At the cylinder surface, located at $\tilde{r} = 1/\beta$, we impose a no-slip boundary condition such that the dimensionless azimuthal velocity is as follows:

$$\tilde{u}_\theta |_{r=R} = \frac{\Omega R}{u_N} = \frac{\text{Ek}}{\text{Re}}, \tag{12}$$

in which Ek is the Ekman number given by

$$\text{Ek} = \frac{\rho (\Omega R) h_N}{\mu}, \tag{13}$$

and $\beta \equiv h_N / R$. Outflow boundary conditions are imposed at the outlet and gas boundary, and thus properties have zero gradient at these boundaries. At the inlet a uniform velocity is applied such that

$$\mathbf{u}(r, \theta, t)|_{z=0} = u_N \hat{\mathbf{z}}, \quad h(t)|_{z=0} = h_N. \tag{14}$$

In dimensional terms, the flow is initiated as a stationary film with thickness h_N, such that

$$\mathbf{u}(r, \theta, z)|_{t=0} = 0, \quad h|_{t=0} = h_N. \tag{15}$$

Here h_N and u_N correspond to the Re given below. A $90°$ sector of the cylinder was used with periodic boundary conditions in the azimuthal direction so as to reduce the computational requirement. The choice of sector size was validated against numerical solutions obtained for a full cylinder. As will be shown below, the computational domain is sufficiently large so as to accommodate the fine-scale features of the emergent waves. The waves have sufficiently small wavelengths in the azimuthal direction to support the choice of utilizing a cylindrical sector with periodic boundary conditions.

In order to simulate rotation within a two-dimensional domain it is necessary to be in the rotating frame of reference. The Navier-Stokes equations can be expressed in a noninertial frame using a Lagrangian approach [42]. We can then model the system in the r-z plane, accounting for the rotation through the reference frame. For this approach to be valid one must take into account the curvature of the cylinder. Chen *et al.*

[32] found that the influence of the curvature on stability was negligible for $1/\beta \gg 10$; in the present case, $1/\beta = 146$, which demonstrates the validity of our approach. Likewise, the centrifugal acceleration varies marginally across the film since β is small. Equation (2) can be reexpressed as follows in a rotating reference frame:

$$\rho\left(\frac{\partial \mathbf{u}'}{\partial t} + \mathbf{u}' \cdot \boldsymbol{\nabla}\mathbf{u}'\right) = -\boldsymbol{\nabla}p + \mu\nabla^2\mathbf{u}' + \rho g\hat{\mathbf{z}} + \sigma\kappa\mathbf{n}\delta$$
$$- \boldsymbol{\Omega} \times (\boldsymbol{\Omega} \times r) - 2\boldsymbol{\Omega} \times \mathbf{u}', \quad (16)$$

where $\boldsymbol{\Omega} = -\Omega\hat{\mathbf{z}}$. Velocity is in the rotating reference frame such that $\mathbf{u}' = \mathbf{u} - \Omega\mathbf{r}$. The fifth and sixth terms on the right-hand side of Eq. (16) correspond to the centrifugal and Coriolis forces, respectively. Substitution of the scalings in Eq. (7) into Eq. (16) yields

$$\frac{\partial \tilde{\mathbf{u}}'}{\partial \tilde{t}} + \tilde{\mathbf{u}}' \cdot \tilde{\boldsymbol{\nabla}}\tilde{\mathbf{u}}' = -\tilde{\boldsymbol{\nabla}}\tilde{p} + \frac{1}{\mathrm{Re}}\tilde{\nabla}^2\tilde{\mathbf{u}}' + \frac{1}{\mathrm{Fr}^2}\hat{\mathbf{z}} + \frac{1}{\mathrm{We}}\tilde{\kappa}\tilde{\boldsymbol{\delta}}$$
$$- \frac{\mathrm{Ek}}{\mathrm{Re}}\left\{\beta^2\left(\frac{\mathrm{Ek}}{\mathrm{Re}}\right)[\hat{\mathbf{z}} \times (\hat{\mathbf{z}} \times \tilde{\mathbf{r}})] + 2(\hat{\mathbf{z}} \times \tilde{\mathbf{u}}')\right\}. \quad (17)$$

The two-dimensional domain encompasses $0 \leqslant z \leqslant L_z$ and $R - L_h \leqslant r \leqslant R$ in the axial and radial directions, respectively. A dimensionless domain size of $\tilde{L}_h \approx 7.5$ and $\tilde{L}_z \approx 725$ minimized the effect of the gas dynamics on the interface and ensured that there was sufficient space for the transition between wave regimes to occur unhindered. Mesh refinement in the region of the film, $\frac{1}{\beta} - 2.5 < \tilde{r} < \frac{1}{\beta}$ was performed such that the mesh size was 0.09 in the film region and 0.45 in $\tilde{z}$, broadly similar to the 2D domain employed by Gao *et al.* [17]. The 3D case was constructed by extruding the 2D geometry and mesh in the azimuthal direction, producing a cylindrical sector with a mesh size of 0.46 in θ in the region of the film. A dynamic time step was selected such that the Courant number Co < 0.5 was satisfied as per the optimum performance of the solver [40].

An air-water system was used such that the gas phase had density $\rho_g = 1.27$ kg m^{-3} and kinematic viscosity $\nu_g = 1.42 \times 10^{-5}$ m^2 s^{-1}. The liquid film has density $\rho_l = 1000$ kg m^{-3}, kinematic viscosity $\nu_l = 1.14 \times 10^{-6}$ m^2 s^{-1}, and surface tension $\sigma_l = 7.28 \times 10^{-2}$ N m^{-1}. The dimensionless parameters based on these conditions are Re = 53, Fr = 4.2, We = 0.18, and $\beta = 1.4 \times 10^{-4}$ while Ek varies between $0 \leqslant \mathrm{Ek} \leqslant 484$.

III. TWO-DIMENSIONAL SIMULATION

A. Direct numerical simulations using VoF

Figure 2 depicts the flow characteristics of a typical film evolution for Ek = 193, which corresponds to an intermediate rotational speed; the rest of the parameter values are fixed at Re = 53, Fr = 4.2, and We = 0.18. Small-amplitude perturbations originating near the domain inlet are amplified downstream under the action of gravity leading to a transition from an essentially waveless to a wavy flow regime. The structure of the emergent waves shown in the time-space
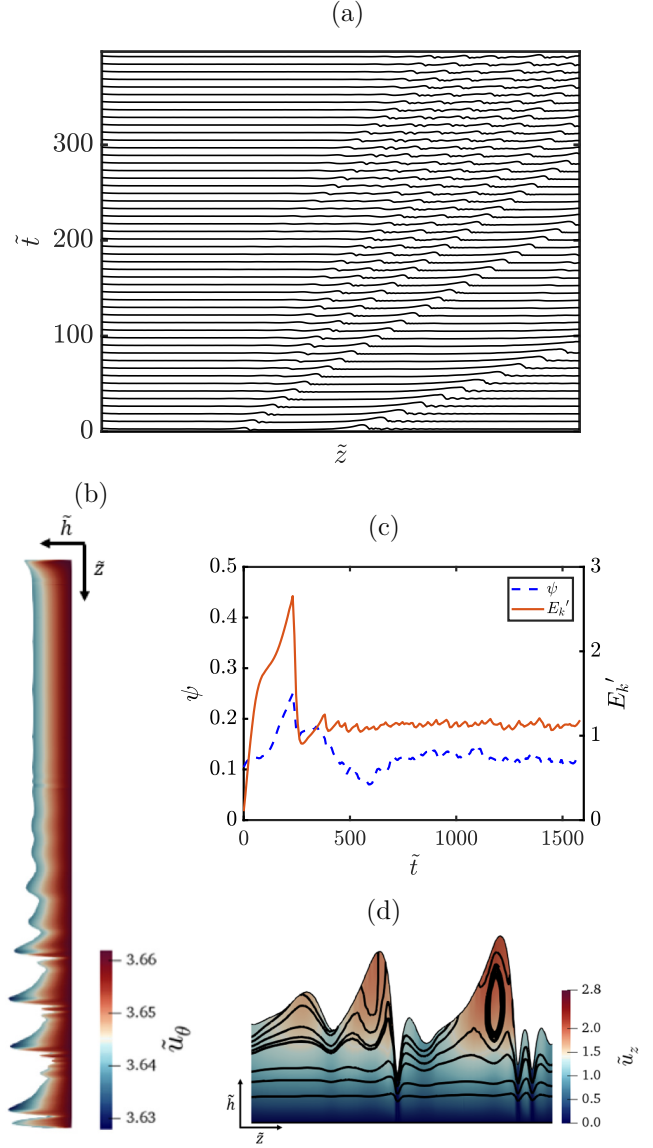

FIG. 2. Flow dynamics for the Ek = 193 case: (a) time-space plot of interface showing a transition toward the point at which the temporal evolution of the interface does not vary significantly; (b) a snapshot of the film thickness profile at $\tilde{t} = 1540$ with the color bar showing the magnitude of the azimuthal velocity component, $\tilde{u}_\theta$; (c) temporal evolution of the kinetic energy, E_k', and film waviness, ψ; d) axial velocity component $\tilde{u}_z$ with streamlines in the reference frame of the wave celerity, c, for $\tilde{t} = 1540$. The rest of the parameters are Re = 53, Fr = 4.2, and We = 0.18.

plot and the snapshot at $\tilde{t} = 1540$ in Figs. 2(a) and 2(b), respectively, is due to a delicate interplay between gravitational, centrifugal, capillary, inertial, and viscous forces. This structure is characterized by large-amplitude features that interact as they flow in the streamwise direction. It is also clear on close inspection of Fig. 2(b) that the magnitude of the azimuthal velocity component, $\tilde{u}_\theta$, in the film varies over a relatively narrow range, close to the imposed cylinder rotation.

In Fig. 2(c) we track the kinetic energy, $E_k{'}$, and the film waviness, ψ, respectively, given by

$$E_k = 2\pi \int_0^{\tilde{L}_z} \int_{1/\beta - \tilde{h}}^{1/\beta} \tilde{r}|\tilde{\mathbf{u}}'|^2 d\tilde{r} d\tilde{z}, \qquad (18)$$

$$\psi = \int_0^{\tilde{L}_z} |\tilde{h} - 1| d\tilde{z}, \qquad (19)$$

where E_k is the kinetic energy in a rotating frame of reference and $E_k{'} = E_k/2\pi$. The film waviness ψ is defined as a measure of the fluctuations of the film from the Nusselt film height. Figure 2(c) shows clearly the point at which the temporal evolution of the flow characteristics begin to plateau after approximately $\tilde{t} = 600$ (though there remain low-amplitude fluctuations in ψ past this point in time).

The time-space plot depicted in Fig. 2(a) can be used to estimate the wave speed or celerity, c, by tracking a single wave in the domain and noting the distance moved Δz in time Δt. This was found to be approximately 0.4 m s^{-1} essentially independent of Ek and, in turn, of the rotational speed of the cylinder, which acts in the azimuthal direction; it is primarily influenced by the constant gravitational force in the axial direction. In some cases, the local wave speed can exceed c leading to the formation of a recirculation zone in the reference frame of the wave celerity [20,43], which gives rise to enhanced mixing. These flow characteristics are less prevalent at high Ek as the impact of rotation mitigates the formation of large, fast waves due to the increased stabilization. This is industrially relevant, as operating at higher rotational speeds may be preferential for certain applications for transport control, for instance, but will demote mixing within the waves. Streamlines in the reference frame of the wave celerity are plotted in Fig. 2(d) where the recirculation zone is clear in the larger, faster-moving wave but absent in the smaller one.

Having analyzed the flow for a single intermediate Ek value, Fig. 3 shows the effect on the dynamics across a range of Ek with all other parameters kept constant at Re = 53, Fr = 4.2, We = 0.18, and $\beta = 6.9 \times 10^{-3}$. Time-space plots of the simulation ($\tilde{t} > 800$) are shown for Ek = 0 in Fig. 3(a) and Ek = 339 in Fig. 3(b), and while the natural evolution from a waveless to a wavy regime is notable in both cases, there are distinct differences. Qualitatively the reduction in the degree of waviness is apparent due to the stabilizing effect. There is also a clear extension in the waveless regime with an increase in Ek, which can be quantified by estimating the transition from the waveless to a wavy regime, beyond a length L_{2D} computed according to $\tilde{z} = L_{2D}$, if $\tilde{h} < 0.98$ or $\tilde{h} > 1.02$. As shown qualitatively in Figs. 3(a) and 3(b), this entry length, establishing the onset of 2D waves, increases monotonically with Ek. This length will be dependent on the relative acceleration in both the centrifugal and axial directions, $\Omega^2 R$ and g, respectively. Therefore, one expects L_{2D} to have the following dependence on the operating parameters:

$$\frac{L_{2D}}{h_N} \sim \frac{\Omega^2 R}{g}. \qquad (20)$$

From the definition of Ek, Re, h_N, and β, this relation can be reexpressed as follows:

$$\frac{L_{2D}}{h_N} \sim \beta \frac{Ek^2}{Re}, \qquad (21)$$

thus $L_{2D} \sim Ek^2$ for fixed β and Re.

The dynamic evolution of $E_k{'}$ and ψ for a range of Ek is also shown in Figs. 3(c) and 3(d), respectively. It is seen clearly that variation of Ek has a profound effect on the film waviness: We observe that there is a decrease in the film waviness with an increase in Ek. At the largest Ek examined, the film waviness is suppressed significantly, with ψ approaching a steady value close to zero, compared with lower Ek. This is as expected as an increase in Ek is tantamount to an increase in the rotational speed, which increases the centrifugal force, stabilizing the flow. In contrast, the temporal variation of $E_k{'}$ is weakly dependent on Ek though it provides an indication of when the temporal evolution of the flow characteristics plateau (beyond $\tilde{t} \approx 500$).

In Fig. 4(a), we show a comparison of waves formed at different Ek with the rest of the parameters kept unaltered from Fig. 3; each one of these waves corresponds to a traveling wave extracted from the domain at distances beyond L_{2D}. The first observation that can be made is the decrease in the amplitude of the wave peaks with an increase in Ek, due to the increasing stabilizing force. It is also seen that at high Ek the wave structure is altered significantly with a severe depression in the peak and a much less pronounced distinction between the primary wave and the capillary waves downstream, which is characteristic of solitary waves in falling film flows. It should be noted that the wave depicted for Ek = 484 in Fig. 4(a), however, does not belong to the nearly sinusoidal wave family but a solitary one. Indeed, we have found that the centrifugal forces arising from the imposed rotation simply delay the emergence of the solitary waves, which is in accordance with the observation made in Fig. 3(e) that illustrates the monotonic growth of L_{2D} with Ek. Further investigation into the nature of fully developed waves is conducted below.

Due to the complex nature of the waves, one would expect the velocity profiles within the thin films to be nonparabolic [44]. We show in Figs. 4(b)–4(f) the shape of these profiles at the designated points in Fig. 4(a). Inspection of Fig. 4(b) reveals that the velocity profiles are close to parabolic upstream of the wave peaks, in the region in the which a flat film is approached. This is in contrast to Fig. 4(c), where profile 3 specifically bulges over the parabolic curve. This feature still exists for Ek = 97 in Fig. 4(e), though to a lesser extent, reflecting the stabilizing effect of cylinder rotation that promotes more parabolic-type profiles. This trend is also apparent on inspection of the profiles within the capillary waves, shown in Figs. 4(d) and 4(f), with the profiles tending toward the parabolic reference curve with increasing Ek. The profiles can also be used to determine the extent of recirculation within the wave. In Figs. 4(c) and 4(e), profiles 2 and 3 bulge below and above the parabolic profile, respectively, and cross one another, indicative of a recirculation zone within the wave, a common feature of solitary wave profiles [17].

We have also performed fast Fourier transforms (FFT) of the time-averaged interface profiles in the wavy regime (for
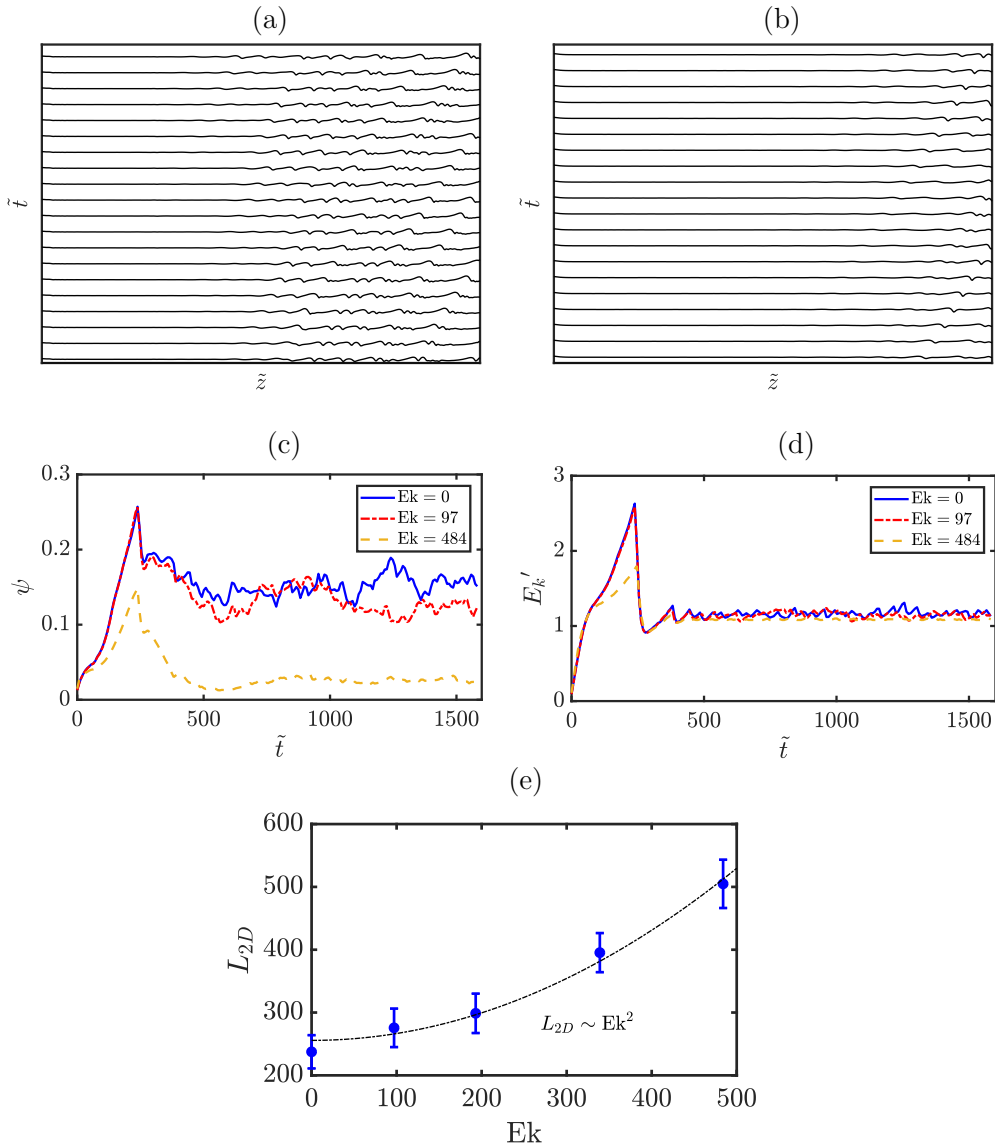
FIG. 3. Effect of Ek on the flow: [(a) and (b)] Time-space plots of the interface for Ek $= 0$ and 484, respectively; [(c) and (d)] temporal evolution of the film waviness, ψ, and kinetic energy, $E_k{'}$, respectively, for Ek $= 0$, 97, and 484; (e) variation of the domain length beyond which a transition to 3D structures is observed, L_{2D}, with Ek. The rest of the parameter values remain unaltered from Fig. 2.

$z > L_{2D}$ for every Ek value considered) after subtracting the mean film height; this is shown in Fig. 5. This subtraction is to account for the $\nu_z = 0$ m^{-1} wave number that would be prevalent with a signal with a nonzero mean amplitude. The time-averaging was performed for times that exceeded those associated with the establishment of the simulation stabilizing for each Ek. In Figs. 5(a) and 5(b), we show example snapshots of the spatial development of the interface for Ek $= 0$ and Ek $= 339$, with their power spectra shown in Figs. 5(c) and 5(d), respectively. It is clearly seen that the profile associated with Ek $= 0$ are significantly wavier than its higher Ek counterpart, characterized by large-amplitude peaks preceded by high-wave-number capillary waves. This is reflected by the higher-energy content of the wave-number modes, particularly at relatively low ν_z, as demonstrated via comparison of Figs. 5(c) and 5(d). Applying a moving average allows us to compare the power spectra associated with the two Ek values in Fig. 5(e). This shows that the dominant mode is weakly

dependent on Ek though the associated amplitude is larger in the purely falling film case. In Fig. 5(f), we plot the variation of the wave number associated with the dominant mode with Ek. It is seen that the dominant modes have wave numbers that are in the range 65–80 m^{-1} for the range of Ek studied, with no strong dependence on Ek suggesting that the structure in the axial direction is not dominated by the centrifugal forces due to cylinder rotation.

We analyze the flow further in both the z and θ directions by plotting the axial and azimuthal flow rates, which are respectively expressed by

$$\tilde{f}_z = \int_{1/\beta-\tilde{h}}^{1/\beta} \tilde{r}\tilde{u}_z d\tilde{r}, \qquad \tilde{f}_\theta = \int_{1/\beta-\tilde{h}}^{1/\beta} \tilde{r}\tilde{u}_\theta d\tilde{r}, \qquad (22)$$

where $\tilde{u}_z$ and $\tilde{u}_\theta$ denote the axial and azimuthal velocity components, respectively, and $(\tilde{f}_z, \tilde{f}_\theta) = (f_z, f_\theta)/2\pi h_N^2 u_N$. In Fig. 6(a), we plot the axial variation of $\tilde{f}_z$ for the falling film
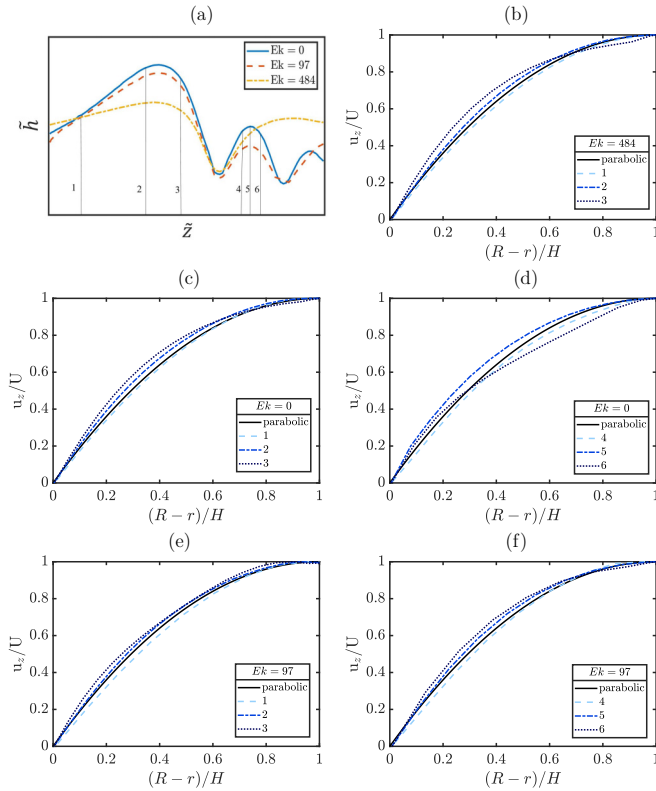
FIG. 4. Velocity profiles in the film underneath the the solitary waves for various Ek with the rest of the parameters remaining unaltered from Fig. 2: (a) three interfacial profiles for Ek = 0, 97, and 484, with the points 1–6 marking the locations at which the radial variation of the axial velocity component normalized by its maximal value, u_z/U, is plotted in (b), (c) and (d), and (e) and (f) for Ek = 484, 0, and 97, respectively; also shown in (b)–(f) is a parabolic profile for reference. The radial coordinate is normalized by the local maximum film height H.
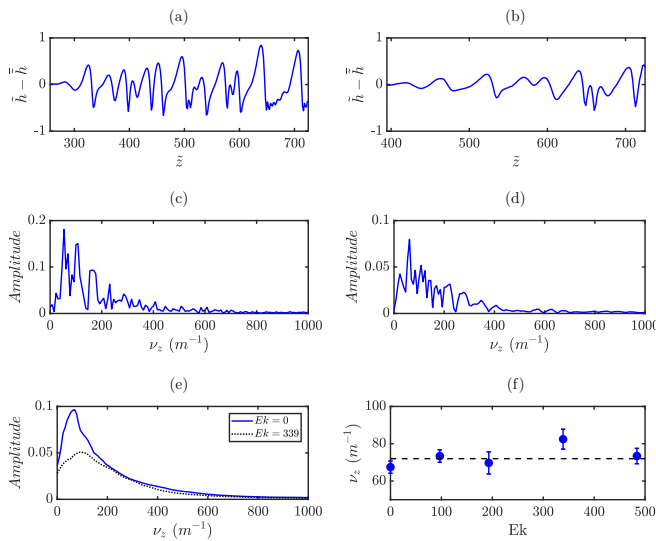

FIG. 5. Single case ($\tilde{t} = 955$) input for FFT for (a) Ek = 0 and (b) Ek = 339; single case FFT output result for (c) Ek = 0 and (d) Ek = 339; (e) time-averaged FFT distributions for Ek = 0 and Ek = 339; (f) time-averaged axial wave number at each Ek. The rest of the parameters remain unchanged from Fig. 2.
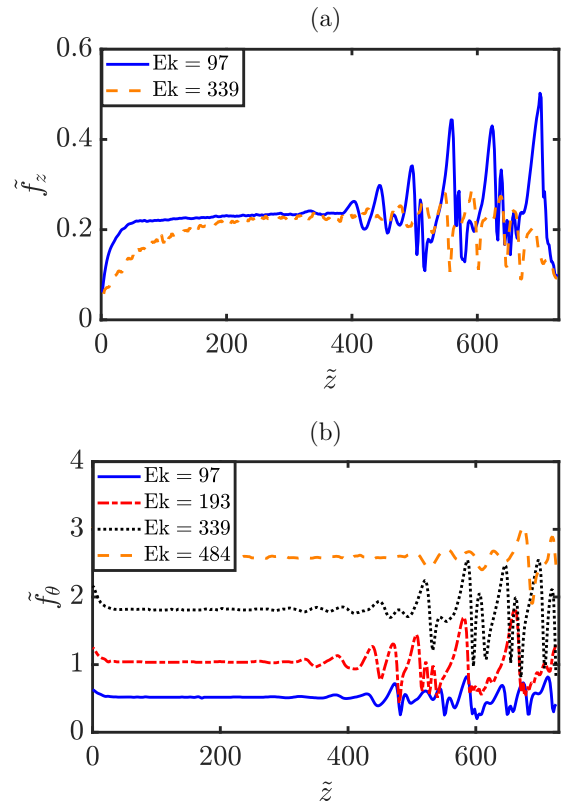

FIG. 6. Axial (a) and azimuthal (b) flow rates for a range of Ek at $\tilde{t} = 1193$. The rest of the parameters remain unaltered from Fig. 2.

and Ek = 339 cases where it is seen that the waviness in $\tilde{f}_z$, which closely relates to that of the interface, is suppressed for the high Ek case; here, the rest of the parameters remain unchanged from Fig. 2. This result is matched by that depicted in Fig. 6(b) in which it is shown that the average $\tilde{f}_\theta$ increases with Ek due to the rise in the influence of centrifugal forces on the flow. Despite this trend, close inspection of Fig. 6(b) also reveals that the amplitude of the oscillations in $\tilde{f}_\theta$ is maximized for an intermediate range of Ek. This is because an increase in Ek results in an increase in $\tilde{u}_\theta$, which promotes $\tilde{f}_\theta$, but also leads to suppression of interfacial waviness. These competing effects give rise to the results presented in Fig. 6(b).

B. Simulations using WRIBL method

The presence of recirculation is an important feature of falling films, with relevance in industrial applications due to enhanced mixing. We have shown that the presence of rotation has a marked effect on the shape of the waves and hence the degree and presence of recirculation. The interplay between the inertial instability in the axial direction and the centrifugal stabilization determines the wave formation. It is instructive to construct a phase diagram with these parameters determining whether recirculation is present, for which we require a model to optimize processing time, compared to the use of full DNS. Rohlfs *et al.* [45] have recently developed *WaveMaker*, a Matlab-based software, which simulates periodic waves in 2D and 3D domains, utilizing a WRIBL approach. In *WaveMaker*, to replicate flow
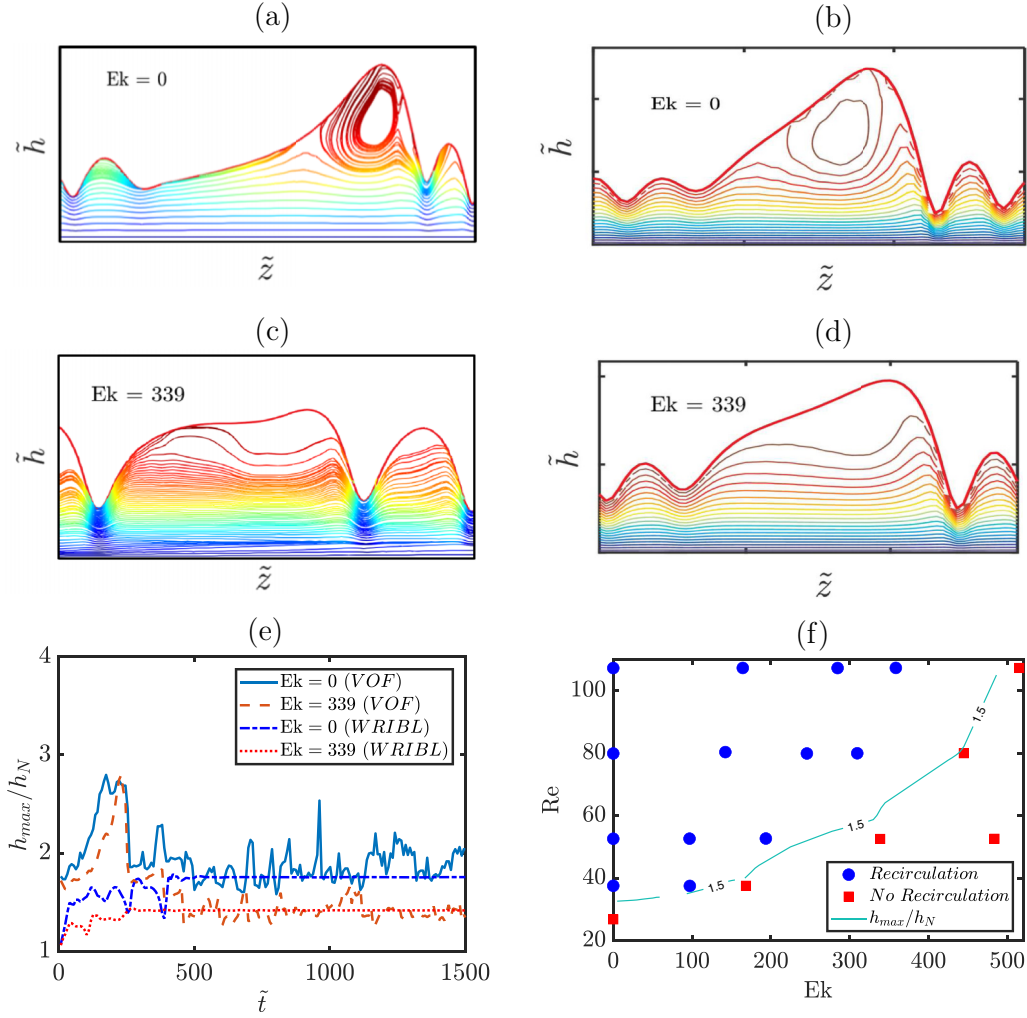
FIG. 7. Comparison of 2D wave formation for (a) VOF, Ek = 0; (b) WRIBL, Ek = 0; (c) VOF, Ek = 339; and (d) WRIBL, Ek = 339; (e) temporal evolution of the maximum film height normalized by the Nusselt film thickness, $h_{\max}/h_N$, generated via the VOF and WRIBL methods; (f) Re-Ek phase diagram showing the boundary separating waves wherein recirculation is observed in a frame-of-reference moving with the wave celerity and for which $h_{\max}/h_N \approx 1.5$. The rest of the parameters remain unaltered from Fig. 2.

on the surface of a rotating cylinder, the flow is subjected to gravitational acceleration in the streamwise and cross-stream directions equaling standard gravitational acceleration and centrifugal acceleration, respectively [45], whereby Coriolis force is neglected compared to the two-dimensional DNS performed above; however, it should be noted that the Coriolis force is often considered neglibible at small scales [46]. Both two-dimensional and three-dimensional domains are utilized and compared to the results from the VOF DNS approach, with the 2D full second-order WRIBL model used to construct a phase diagram in Re-Ek space.

One notes that the VOF simulations are of a developing wave and are periodic in the azimuthal direction, compared to the WRIBL model, which is for spatially periodic waves in both the streamwise and spanwise directions. However, a comparison can be made between more developed waves in the latter part of the domain $\tilde{z} > L_{2D}$ and those created via the WRIBL approach. A domain size of 0.0143 m was chosen based on an axial wave number that has been shown to be $\nu_z \approx 70$ m^{-1} for the range of Ek investigated in Fig. 5(f). We employ the analogy that the simulation in the case of a

film on the inside of a rotating cylinder corresponds to that of its counterpart on a plane inclined at an angle γ set by $\gamma = \tan^{-1}(g/\Omega^2 R)$. For a chosen Ek value, the corresponding Ω is then used to determine γ whence the Reynolds number for the inclined plane WRIBL simulation is given by

$$\text{Re}_{\text{WRIBL}} = \frac{h_N^3}{3\nu^2} g \sin\gamma. \qquad (23)$$

It is important to check the curvature of the cylinder in the VOF simulations is such that an inclined plane analogy is valid. As stated previously the curvature $1/\beta \gg 10$ making the influence of the curvature on the stability negligible [32].

Figures 7(a) and 7(b) provide a comparison for Ek = 0 of the 2D waves from the VOF and WRIBL simulations, respectively. With no centrifugal force suppressing wave formation, the recirculation within the solitary wave is evident. Furthermore, the capillary waves are significantly smaller than the preceding main hump. In contrast, at Ek = 339, as observed in Fig. 7(c) and Fig. 7(d), recirculation is absent from the main wave hump. We then compare the WRIBL results to those obtained from the VOF simulations in terms of
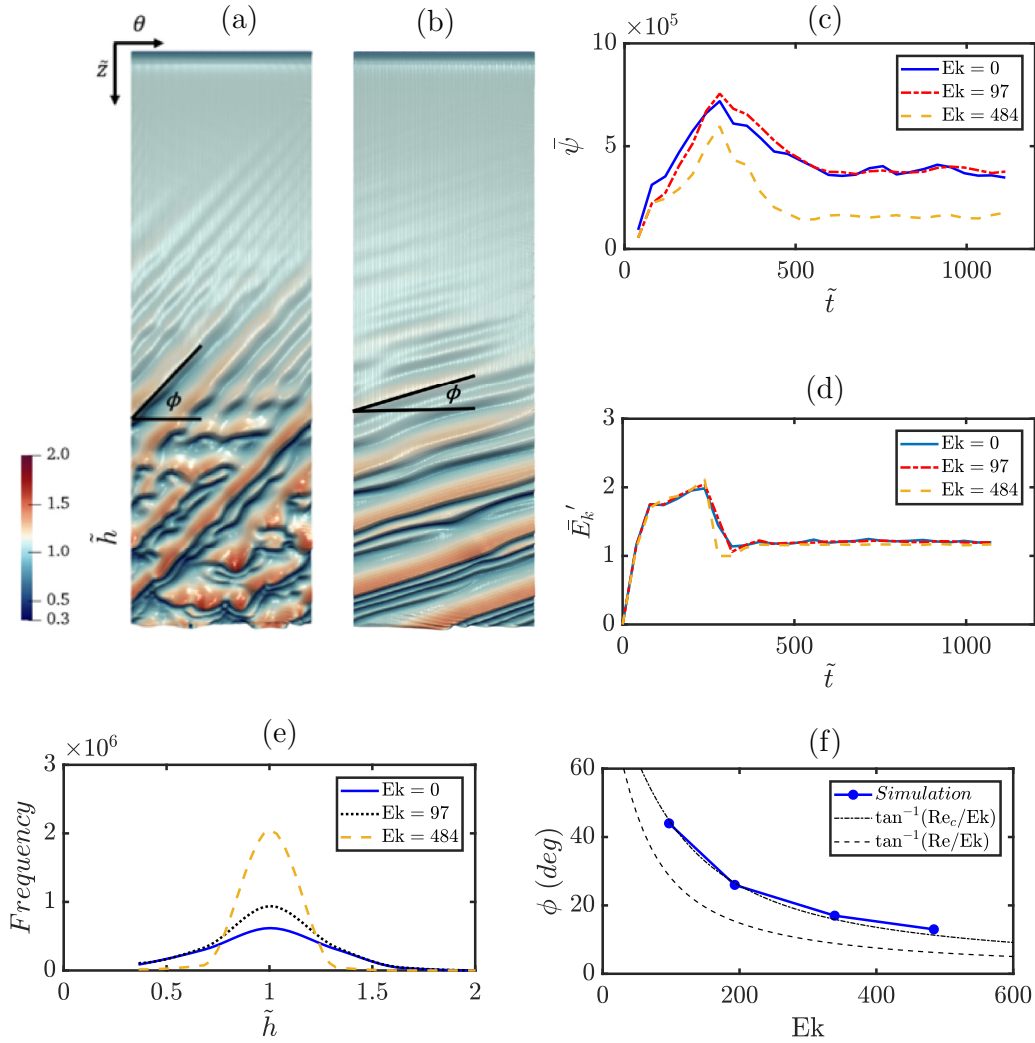
FIG. 8. Snapshots taken at $\tilde{t} = 955$ showing contour plots of the interface that demonstrate the formation of angled waves for (a) Ek = 97 and (b) Ek = 339; dynamic evolution of the film waviness ψ and kinetic energy $E_k{'}$, shown in (c) and (d), respectively, for a range of Ek; (e) narrowing of the film height distribution with an increase in Ek. The rest of the parameters remain unaltered from Fig. 2; (f) comparison of the angle ϕ values obtained from simulations with those determined from Eq. (26) with $\mathcal{U}$ from extracted wave celerities and Nusselt theory.

temporal evolution of the maximal film thickness normalized by the Nusselt film thickness, h_{max}/h_N. Figure 7(e) shows that the WRIBL results converge to a steady state, with a lower h_{max}/h_N for the higher Ek case, due to the increased stability. This h_{max}/h_N for each Ek matches well with the quasi–steady state obtained from the VOF simulations, suggesting that the developed waves where $\tilde{z} \gg L_{2D}$ are comparable to those obtained by the WRIBL model, further supported qualitatively through Figs. 7(a)–7(d). These results indicate that the WRIBL approach provides a reasonably good approximation of the VOF DNS predictions. On this basis, the WRIBL method was used to construct the phase diagram shown in Fig. 7(f). Notably, the level of inertia, characterized by Re, required to have recirculation increases with Ek. The critical boundary for recirculation in Re-Ek space coincides with the $h_{max}/h_N = 1.5$ contour; thus, the latter provides an effective criterion for the onset of recirculation. As will be discussed below, this can be applied in the three-dimensional case to

determine the presence of recirculation, to which we now turn our attention.

IV. THREE-DIMENSIONAL SIMULATIONS

In this section, we present the results of our 3D simulations of the interfacial dynamics. Our aim is to uncover details of the flow masked by the axisymmetric assumption made in the previous section; details of the simulation setup are found in Sec. II. In Figs. 8(a) and 8(b), we show snapshots of the interface in the "unwrapped" (θ, z) plane for Ek = 97 and Ek = 339, respectively, wherein the color represents the thickness of the film. Similarly to the 2D predictions discussed in Sec. III, these figures show clearly the development of a wavy interface from an essentially waveless region near the domain inlet. In 3D, however, it is seen that the effect of rotation causes the formation of waves that appear to be oriented to the horizontal with a reasonably well-defined angle ϕ. In Fig. 8(c), it is seen

that the film waviness, $\bar{\psi}$, decreases with Ek, just as in the 2D case, and its temporal variation reaches a steady state beyond a dimensionless time whose value is not a strong function of Ek. In Fig. 8(d), we also see that the kinetic energy, which, just as in the 2D case, is weakly dependent on Ek, also reaches a steady-state albeit at an earlier time than $\bar{\psi}$. Here $\bar{\psi}$ and $\bar{E_k}' = \bar{E_k}/2\pi$ represent the film waviness and kinetic energy, in the fully three-dimensional domain:

$$\bar{\psi} = \int_0^{\pi/2} \int_0^{\tilde{L}_z} |\tilde{h} - 1| d\tilde{z} d\theta, \tag{24}$$

$$\bar{E_k} = 2\pi \int_0^{\pi/2} \int_0^{\tilde{L}_z} \int_{1/\beta-\tilde{h}}^{1/\beta} \tilde{r} |\tilde{\mathbf{u}}'|^2 d\tilde{r} d\tilde{z} d\theta. \tag{25}$$

The distribution of film heights is also obtained from the 3D simulations and shown in Fig. 8(e). We observe a narrowing of the distribution around the Nusselt film height as Ek increases due to the stabilizing effect of an increase in the rotational speed, as the suppression of wave formation reduces fluctuations around h_N. The "angled" waves occur due to a competition between the axial flow due to gravity and the azimuthal flow due to the rotation of the cylindrical surface. On this basis, we propose an expression that provides an estimate of the angle, ϕ_a, which assumes the direction of mean wave motion to be aligned with that of the resultant of axial and azimuthal characteristic velocities, $\mathcal{U}\hat{\mathbf{z}}$ and $\mathcal{V}\hat{\boldsymbol{\theta}}$, respectively:

$$\phi_a = \tan^{-1}\left(\frac{\mathcal{U}}{\mathcal{V}}\right), \tag{26}$$

where $\hat{\mathbf{z}}$ and $\hat{\boldsymbol{\theta}}$ denote the unit vectors in the axial and azimuthal directions, respectively, $\mathcal{V} = \Omega R$, and a reasonable estimate for $\mathcal{U}$ is given by the wave celerity that can be extracted readily from the time-space plots in the 2D simulations. In Fig. 8(f), we plot the variation of ϕ with Ek, where it can be seen that ϕ decays as a function of Ek. If one were to choose the Nusselt solution, u_N, for $\mathcal{U}$ then using the definitions for Re and Ek, it is seen readily that $\tan\phi_a = \text{Re}/\text{Ek}$, thus $\tan\phi_a \sim \text{Ek}^{-1}$ for fixed Re. This corresponds to the assumption that the falling film has a uniform film thickness. As can be seen from Fig. 8(f), this approximation gives rise to a similar qualitative trend to that already discussed but a significant quantitative discrepancy; the latter is attributed to the presence of the waves, which are not taken into account in the Nusselt solution. Also shown in Fig. 8(f) is the prediction from Eq. (26) utilizing the wave celerity, c, whereby $\text{Re}_c = \frac{\rho c h_N}{\mu}$, which shows excellent agreement with those obtained from the 3D numerical simulations.

We perform two-dimensional FFTs of the interface contour in the (θ, z) plane, as shown in Fig. 9(a), with the contour plot of the power spectra shown in Fig. 9(b); here ν_z and ν_θ denote the wave numbers in the axial and azimuthal directions, respectively. The discrete Fourier transform Y of an m-by-n matrix X is given by:

$$Y_{p+1,q+1} = \sum_{j=0}^{m-1} \sum_{k=0}^{n-1} \omega_m^{jp} \omega_n^{kq} X_{j+1,k+1}, \tag{27}$$
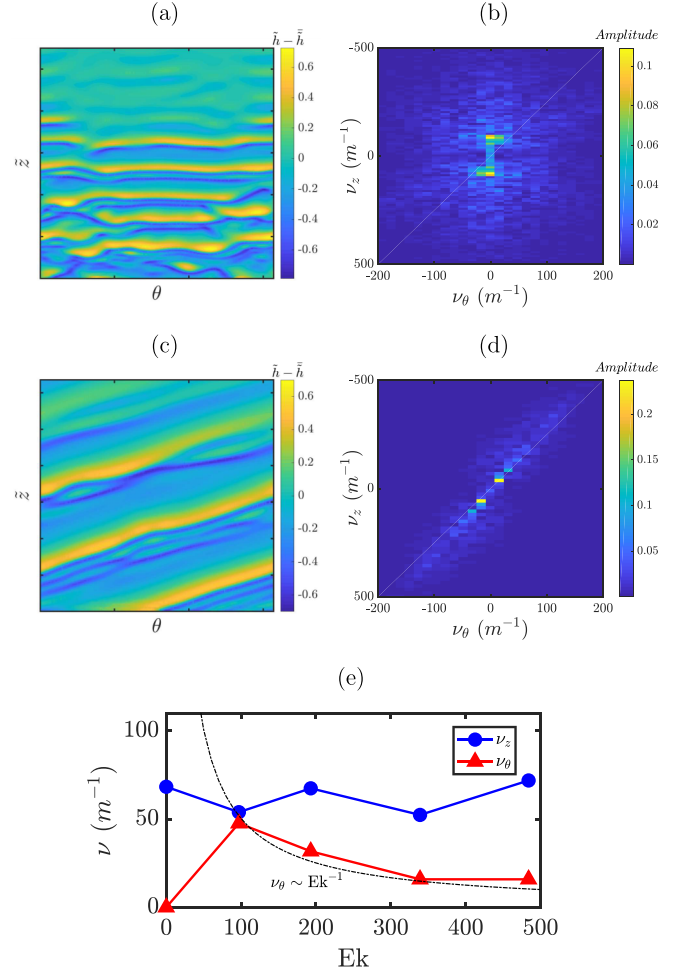

FIG. 9. (a) Input signal to 2D FFT for Ek = 0; (b) FFT output of Ek = 0 case; (c) input signal to 2D FFT for Ek = 339; (d) FFT output of Ek = 0 case; (e) variation of axial and azimuthal wave numbers, ν_z and ν_θ, with Ek. The rest of the parameters remain unaltered from Fig. 2.

where ω_m and ω_n are complex roots of unity:

$$\omega_m = e^{-2\pi i/m}, \quad \omega_n = e^{-2\pi i/n}, \tag{28}$$

i is the imaginary unit, p and j are indices that span 0 to $m - 1$, and q and k are indices that span 0 to $n - 1$. Here the $m \times n$ input is the matrix of film heights in the (θ, z) plane. We require similar modifications to the input as in the 2D case, in order to avoid biasing the result via the waveless section of the flow or through the nonzero mean amplitude bias inherent within the FFT. As seen in Fig. 9(a), we modify the input using L_{2D} and $\tilde{h} - \bar{\tilde{h}}$, for this case Ek = 0. After applying the FFT, the result is mapped onto the (ν_θ, ν_z) plane, as shown in Fig. 9(b), where the peak of maximum amplitude is highlighted in yellow. From Fig. 9(a), we can qualitatively estimate 8 waves within the domain yielding $\nu_z \approx 70 \text{ m}^{-1}$. This coincides with ν_z readings computed from the 2D simulation and the FFT result in Fig. 9(b). We also note in this no-rotation, Ek = 0, case, that the waves are not angled, which is reflected in the FFT result as $\nu_\theta = 0$ at the primary peak, showing the absence of a contribution from the
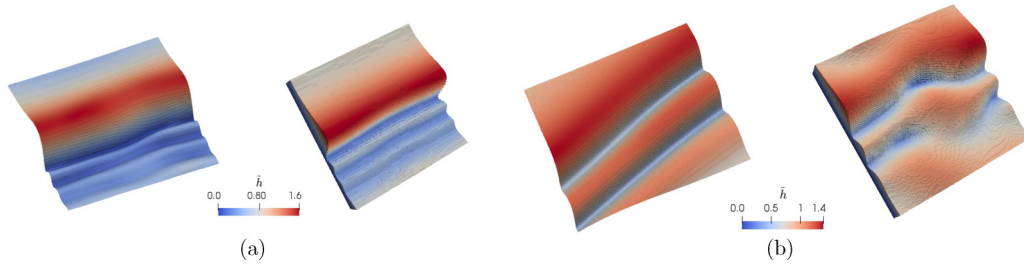
FIG. 10. Comparison of 3D simulations for (a) Ek = 0 and (b) Ek = 339. In each panel the VOF and WRIBL solutions are shown in the left and right panels, respectively. The rest of the parameters are unaltered from Fig. 2.

azimuthal wave number ν_θ. As Ek is increased, the waves become angled leading to a nonzero contribution to ν_θ. An example of this is provided by the Ek = 339 case for which the interface contour is shown in Fig. 9(c). The associated FFT output is shown in Fig. 9(d), with the peak at $\nu_z = 63$ m^{-1} and $\nu_\theta = 16$ m^{-1}. As demonstrated above, the angles of the waves strongly depend on Ek and we expect a similar relationship between Ek and ν_θ. In a similar manner to the results of the FFT for the 2D simulation for which ν_z is weakly dependent on Ek [see Fig. 5(f)], Fig. 9(e) shows that while ν_z remains approximately constant with Ek, ν_θ decreases for Ek > 0 and follows a similar trend to that shown in Fig. 8(e) for angle ϕ vs. Ek. One expects the length scale of a coherent structure in the azimuthal direction, λ_θ, to be the product of a linear velocity set by the cylinder rotation, ΩR, and a timescale set by the gravitational forces, h_N/u_N. From the definitions of Re and Ek, $\lambda_\theta \sim \Omega R h_N/u_N \sim (\text{Ek}/\text{Re})h_N$. Thus, $\lambda_\theta \sim$ Ek and $\nu_\theta \sim \lambda_\theta^{-1} \sim \text{Ek}^{-1}$ for fixed Re.

The full second-order WRIBL can be run in 3D space in order to draw a comparison with the VOF simulations, as in Fig. 7. The 3D domain size was selected in order to obtain a single wave in the domain, similarly to the 2D case, with the exception that it imposes double periodic boundary conditions. Hence, accounting for the wave number computed from the FFT, a 0.0143 m^2 domain was selected. The analogy with a falling film on an inclined plate proposed for the 2D analysis was also employed for this 3D configuration. As stated in Sec. III the comparison is valid for $1/\beta \gg 10$ [32] as is the case here. A developed wave profile from the VOF simulation is compared to that obtained from the WRIBL model in Fig. 10, using the same domain area. The variation in film height in the the Ek = 0 case is much more significant, reflecting the enhanced stability due to rotation. Furthermore, the capillary waves are smaller and more numerous, reflected in both simulations. From Fig. 10(b), we observe the angled waves are not captured using the WRIBL model, as this uses a normal acceleration compared to a physically moving wall. Comparing the maximum film height to the 2D case in Fig. 7 we note that $h_{\max}$ is systematically 5% lower in the 3D case, possibly due to spanwise surface tension interactions. Despite this, after applying the criteria of $h_{\max}/h_N > 1.5$ for recirculation, we yield the same result, with sufficient Ek suppressing wave formation and recirculation, reflected in Fig. 10. While there is a clear difference in the wave orientation with the rotationally resolved DNS in Fig. 10(b), the ability of the WRIBL method to predict the effects of rotation on wave

formation and recirculation in a developed state appears advantageous for rapidly establishing operating conditions for the intensification and control of convective transport within the film.

V. CONCLUSION

We have investigated the flow of a thin film falling under gravity on the inside of a vertical cylinder undergoing steady rotation by studying the interfacial dynamics in two and three dimensions via numerical simulations using the VOF method. We have shown that the cylinder rotation, characterized by an Ekman number has a significant effect on the structure of the interfacial waves. Increasing the relative magnitude of the centrifugal force enhances interfacial stability, suppresses the wave formation brought about by the Kapitza instability and extends the development length from the domain inlet prior to the appearance of the waves. Furthermore, our three-dimensional simulations demonstrate the formation of angled waves where the angle is dependent on the wave celerity and azimuthal velocity. FFT's of the interface are performed in both the two- and three-dimensional cases, finding that the axial wave number is independent of the rotational speed, while the azimuthal wave number is closely aligned with the angle of the waves, and hence decreases with an increase in Ek. We have also compared the predictions from a Matlab-based weighted residual integral boundary-layer method approach [45] to the two- and three-dimensional VOF results and used it to construct a phase diagram, in which we highlighted the regions in Ekman-Reynolds number space wherein recirculation within the wave peaks is expected to arise.

[1] P. L. Kapitza, Wave flow of thin layers of a viscous liquid. Part 1. Free flow, Zh. Eksp. Teor. Fiz. **18**, 3 (1948).

[2] P. L. Kapitza and S. P. Kapitza, Wave flow of thin layers of viscous liquids. Part III. Experimental research of a wave flow regime, Zh. Eksp. Teor. Fiz. **19**, 105 (1949).

[3] R. V. Craster and O. K. Matar, Dynamics and stability of thin liquid films, Rev. Mod. Phys. **81**, 1131 (2009).

[4] S. Kalliadasis, C. Ruyer-Quil, B. Scheid, and M. Velarde, *Falling Liquid Films* (Springer, Berlin, 2012).

[5] G. F. Dietze, On the Kapitza instability and the generation of capillary waves, J. Fluid Mech. **789**, 368 (2016).

[6] V. Patnaik and H. Perez-Blanco, Roll waves in falling films: An approximate treatment of the velocity field, Int. J. Heat Fluid Flow **17**, 63 (1996).

[7] S. Alekseenko, V. Antipin, A. Cherdantsev, S. Kharlamov and D. Markovich, Two-wave structure of liquid film and wave interrelation in annular gas-liquid flow with and without entrainment, Phys. Fluids **21**, 061701 (2009).

[8] S. Alekseenko, A. Cherdantsev, M. Cherdantsev, S. Isaenkov, S. Kharlamov and D. Markovich, Application of a high-speed laser-induced fluorescence technique for studying the three-dimensional structure of annular gas-liquid flow, Exp. Fluids **53**, 77 (2012).

[9] J. Liu and J. P. Gollub, Onset of Spatially Chaotic Waves on Flowing Films, Phys. Rev. Lett. **70**, 2289 (1993).

[10] J. Liu, J. D. Pauk and J. P. Gollub, Measurements of the primary instabilities of film flows, J. Fluid Mech. **250**, 69 (1993).

[11] I. Zadrazil, O. K. Matar and C. N. Markides, An experimental characterization of downwards gas-liquid annular flow by laser-induced fluorescence: Flow regimes and film statistics, Int. J. Multiphase Flow **60**, 87 (2014).

[12] I. Zadrazil and C. N. Markides, An experimental characterization of liquid films in downwards co-current gas-liquid annular flow by particle image and tracking velocimetry, Int. J. Multiphase Flow **67**, 42 (2014).

[13] A. Charogiannis, J. S. An, and C. N. Markides, A simultaneous laser-induced fluorescence, particle image velocimetry and particle tracking velocimetry technique for the investigation of liquids film flows, Exp. Therm. Fluid Sci. **68**, 516 (2015).

[14] C. Ruyer-Quil and P. Manneville, Improved modeling of flows down inclined planes, Eur. Phys. J. B **15**, 357 (2000).

[15] B. Scheid, C. Ruyer-Quil, and P. Manneville, Wave patterns in film flows: Modeling and three dimensional waves, J. Fluid Mech. **562**, 183 (2006).

[16] B. Ramaswamy, S. Chippada, and S. W. Joo, A full-scale numerical study of interfacial instabilities in thin-film flows, J. Fluid Mech. **325**, 163 (1996).

[17] D. Gao, N. B. Morley, and V. Dhir, Numerical simulation of wavy falling film flow using VOF method, J. Comput. Phys. **192**, 624 (2003).

[18] T. Nosoko and A. Miyara, The evolution and subsequent dynamics of waves on a vertically falling liquid film, Phys. Fluids **16**, 1118 (2004).

[19] C. D. Park, T. Nosoko, S. Gima, and S. T. Ro, Wave-augmented mass transfer in a liquid film falling inside a vertical tube, Int. J. Heat Mass Transf. **47**, 2587 (2004).

[20] F. Denner, A. Charogiannis, M. Prads, C. N. Markides, B. G. M. van Wachem, and S. Kalliadasis, Solitary waves on falling liquid films in the inertia-dominated regime, J. Fluid Mech. **837**, 491 (2018).

[21] G. F. Dietze, W. Rohlfs, K. Nahrich, and B. Scheid, Investigation of the backflow phenomenon in falling liquid films, J. Fluid Mech. **595**, 435 (2008).

[22] N. A. Malamataris and V. Balakotaiah, Flow structure underneath the large amplitude waves of a vertically falling film, AIChE J. **54**, 1725 (2008).

[23] R. M. Roberts and H.-C. Chang, Wave-enhanced interfacial transfer, Chem. Eng. Sci. **55**, 1127 (2000).

[24] C. Albert, H. Marschall, and D. Bothe, Direct numerical simulation of interfacial mass transfer into falling films, Int. J. Heat Mass Transf. **69**, 343 (2014).

[25] K. Stephan, Heat transfer in falling film evaporators, in *Heat Transfer in Condensation and Boiling*, International series in heat and mass transfer (Springer, Berlin, 1992).

[26] S. Yanniotis and D. Kolokotsa, Experimental study of water vapour condensation on a rotating disk, Int. Commun. Heat Mass Transfer **23**, 721 (1996).

[27] H. Chen, Heat transfer and fouling in film evaporators with rotating surfaces, Ph.D. thesis, Massey University, 1997.

[28] T. B. Benjamin, Wave formation in laminar flow down an inclined plane, J. Fluid Mech. **2**, 554 (1957).

[29] C.-S. Yih, Stability of liquid flow down an inclined plane, Phys. Fluids **6**, 321 (1963).

[30] T.-S. Lin and L. Kondic, Thin films flowing down inverted substrates: Two dimensional flow, Phys. Fluids **22**, 052105 (2010).

[31] M. Rietz, B. Scheid, F. Gallaire, N. Kofman, R. Kneer, and W. Rohlfs, Dynamics of falling films on the outside of a vertical rotating cylinder: Waves, rivulets and dripping transitions, J. Fluid Mech. **832**, 189 (2017).

[32] C. I. Chen, C. K. Chen, and T. Y. Yang, Pertubation analysis to the nonlinear stability characterization of thin condensate falling film on the outer surface of a rotating vertical cylinder, Int. J. Heat Mass Transf. **47**, 1937 (2004).

[33] L. A. Davalos-Orozco and G. Ruiz-Chavarria, Hydrodynamic instability of a fluid layer flowing down a rotating cylinder, Phys. Fluids **5**, 2390 (1993).

[34] G. Taylor, The instability of liquid surfaces when accelerated in a direction perpendicular to their planes, Proc. R. Soc. Lond. A **201**, 192 (1950).

[35] D. H. Sharp, An overview of Rayleigh-Taylor instability, Physica D **12**, 3 (1984).

[36] G. Ruiz-Chavarria and L. A. Davalos-Orozco, Stability of a liquid film flowing down a rotating cylinder subject to azimuthal disturbances, J. Phys. II, **6**, 1219 (1996).

[37] Y. Iwasaki and E. Hasegawa, Stability of a liquid layer down the durface of a vertical rotating cylinder, Bull. JSME **24**, 54 (1981).

[38] J. U. Brackbill, D. B. Kothe, and C. Zemach, Continuum method for modeling surface tension, J. Comput. Phys. **100**, 335 (1992).

[39] S. S. Deshpande, L. Anumolu, and M. F. Trujillo, Evaluating the performance of the two-phase flow solver interFoam, Comput. Sci. Discov. **5**, 014016 (2012).

[40] J. Roenby, H. Bredmose, and H. Jasak, A computational method for sharp interface advection, R. Soc. Open Sci. **3**, 160405 (2016).

[41] S. Popinet, Numerical models of surface tension, Annu. Rev. Fluid Mech. **50**, 49 (2018).

[42] G. K. Bachelor, *An Introduction to Fluid Dynamics* (Cambridge University Press, New York, 1970), p. 140.

[43] W. Rohlfs and B. Scheid, Phase diagram for the onset of circulating waves and flow reversal in inclined falling films, J. Fluid Mech. **763**, 322 (2015)

[44] N. A. Malamataris, M. Vlachogiannis, and V. Bontozoglou, Solitary waves on inclined films: Flow structure and binary interactions, Phys. Fluids **14**, 1082 (2002).

[45] W. Rohlfs, M. Rietz, and B. Scheid, WaveMaker: The three-dimensional wave simulation tool for falling liquid films, SoftwareX **7**, 211 (2018)

[46] S. Lee, S.-K. Ryi, and H. Lim, Solutions of Navier-Stokes equation with Coriolis force, Adv. Math. Phys. **2017**, 7042686 (2017).